

Unraveling the effects of inter-site Hubbard interactions in spinel Li-ion cathode materials

Iurii Timrov,^{1,*} Michele Kotiuga,¹ and Nicola Marzari¹

¹*Theory and Simulation of Materials (THEOS), and National Centre for Computational Design and Discovery of Novel Materials (MARVEL), École Polytechnique Fédérale de Lausanne (EPFL), CH-1015 Lausanne, Switzerland*
(Dated: March 30, 2023)

Accurate first-principles predictions of the structural, electronic, magnetic, and electrochemical properties of cathode materials can be key in the design of novel efficient Li-ion batteries. Spinel-type cathode materials $\text{Li}_x\text{Mn}_2\text{O}_4$ and $\text{Li}_x\text{Mn}_{1.5}\text{Ni}_{0.5}\text{O}_4$ are promising candidates for Li-ion battery technologies, but they present serious challenges when it comes to their first-principles modeling. Here, we use density-functional theory with extended Hubbard functionals—DFT+ U + V with on-site U and inter-site V Hubbard interactions—to study the properties of these transition-metal oxides. The Hubbard parameters are computed from first-principles using density-functional perturbation theory. We show that while U is crucial to obtain the right trends in properties of these materials, V is essential for a quantitative description of the structural and electronic properties, as well as the Li-intercalation voltages. This work paves the way for reliable first-principles studies of other families of cathode materials without relying on empirical fitting or calibration procedures.

I. Introduction

Over the past 30 years rechargeable Li-ion batteries have been the subject of very active research, driven both by the growing worldwide market of portable electronics and electric vehicles and in order to meet the climate-neutral requirements of our society [1, 2]. Applications demand advanced energy-storage systems with excellent energy density, cyclability, and thermal stability. Among various available cathode materials, lithium-manganese-oxide spinels have attracted special attention due to their low cost, nontoxicity, and higher Li-intercalation voltages than commercial layered rock-salt cathodes [3].

LiMn_2O_4 is the prototypical spinel cathode material [4], having an operating voltage of ~ 4.15 V [5–7] and a high capacity of ~ 140 mA h g^{-1} [8]. This material has a high-temperature cubic phase with space group $Fd\bar{3}m$; however, at low temperatures it is still debated whether the structure is orthorhombic or tetragonal [9–11]. The Mn ions have mixed-valence state consisting of Jahn-Teller (JT) active Mn^{3+} and non-JT active Mn^{4+} ions, and, while these are disordered in the cubic phase, in the low-temperature phase there is charge ordering of these two types of Mn ions [10]. Experimentally it is known that LiMn_2O_4 has an antiferromagnetic (AFM) ground state at low temperatures [12], though the exact type of AFM ordering is not known due to the complex magnetic interactions in this material. However, despite the attractive properties of LiMn_2O_4 as a cathode material, it exhibits degradation with extended cycling, and hence various types of doping (partial Mn substitutions) have been explored in order to enhance the electrochemical performance [13–15]. One candidate that has received a great deal of attention is $\text{LiMn}_{1.5}\text{Ni}_{0.5}\text{O}_4$, as it offers

even higher power capabilities with an operating voltage of ~ 4.7 V and a capacity of ~ 135 mA h g^{-1} [16, 17]. It is known experimentally that $\text{LiMn}_{1.5}\text{Ni}_{0.5}\text{O}_4$ also crystallizes in a spinel phase but in two possible space groups $Fd\bar{3}m$ or $P4_332$ (or $P4_132$, which is an enantiomorph of $P4_332$) depending on the synthesis conditions, and that Ni^{2+} is redox active while Mn^{4+} is inactive [17–19]. This material adopts a ferrimagnetic (FiM) ordering below the Curie temperature (~ 130 K) in which the Mn^{4+} spins align antiparallel to the Ni^{2+} spins [15, 20, 21]. Nonetheless, the commercialization of this material has been hampered by severe capacity fade, particularly at elevated temperatures, in cells employing a graphite anode [17]. Therefore, the need is apparent for in-depth characterization of these materials in order to understand the underlying physical mechanisms and to further improve their electrochemical performance.

LiMn_2O_4 has been extensively studied using density-functional theory (DFT) [23, 24] with semi-local exchange-correlation (xc) functionals augmented with Hubbard corrections, i.e. the so-called DFT+ U approach [25–27]. It has been shown that the on-site Hubbard U correction is crucial to describe the mixed valence state of Mn ions, thus correctly predicting the existence of Mn^{3+} and Mn^{4+} ions and the insulating ground state of this material [7, 28–33]. Moreover, in Ref. [34] it has been shown that various types of hybrid xc functionals correctly describe the ground-state properties of this compound. Among these, Refs. [28, 32, 34] investigated in detail various types of AFM ordering, eventually finding somewhat different lowest-energy spin configurations and showing that various magnetic orderings differ just by a few meV or a few tens of meV per formula unit. Conversely, first-principles studies of $\text{LiMn}_{1.5}\text{Ni}_{0.5}\text{O}_4$ are much scarcer, with Ref. [35] presenting a DFT+ U study of ferromagnetic (FM) $\text{LiMn}_{1.5}\text{Ni}_{0.5}\text{O}_4$ with a primary focus on vibrational and Raman spectral properties. In the majority of these DFT+ U studies of LiMn_2O_4 and

* iurii.timrov@epfl.ch

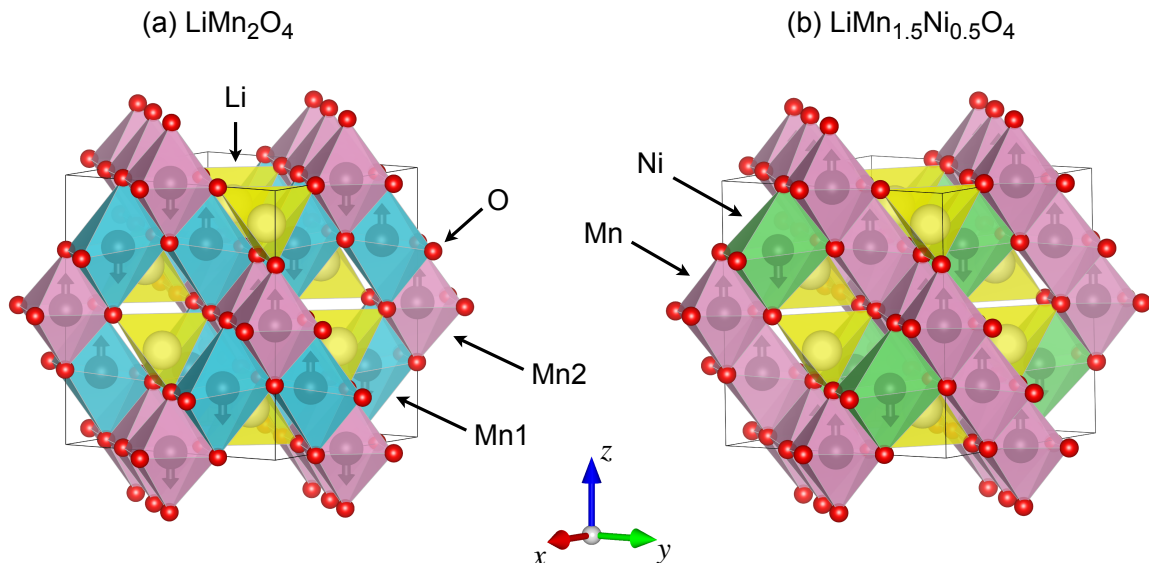


FIG. 1: Crystal structure of spinel cathode materials: (a) LiMn_2O_4 , and (b) $\text{LiMn}_{1.5}\text{Ni}_{0.5}\text{O}_4$. Black thick vertical arrows inside the octahedra indicate the orientation of spin. In (a), two types of Mn ions, Mn1 and Mn2, correspond respectively to Mn^{3+} and Mn^{4+} that were observed experimentally. In (b), there is only one type of Mn ions which corresponds to Mn^{4+} , and there is one type of Ni ions which corresponds to Ni^{2+} . Rendered using VESTA [22].

$\text{LiMn}_{1.5}\text{Ni}_{0.5}\text{O}_4$ the on-site Hubbard U parameter has been chosen empirically such that some experimental properties of interest are well reproduced; this is different from a fully first-principles-based approach and likely contributed to the spread of the reported results. Most importantly, the effect of inter-site Hubbard V interactions [36–38] has never been investigated in the spinel cathode materials; these interactions have been shown to be very important in other transition-metal (TM) oxides due to strong metal-ligand hybridization [39–49].

Herein, we present a fully first-principles study of the structural, electronic, magnetic, and electrochemical properties of the spinel cathode materials $\text{Li}_x\text{Mn}_2\text{O}_4$ and $\text{Li}_x\text{Mn}_{1.5}\text{Ni}_{0.5}\text{O}_4$ ($x = 0$ and 1) using DFT with extended Hubbard functionals (DFT+ U + V) [36], where the on-site U and inter-site V Hubbard parameters are computed unbiasedly and fully from first-principles using density-functional perturbation theory (DFPT) [50, 51] in a basis of Löwdin-orthogonalized atomic orbitals. This avoids any empiricism and possible ambiguities of Hubbard-corrected DFT studies. The Hubbard parameters are determined using the self-consistent procedure prescribed in Refs. [40, 51, 52] to ensure that the crystal and electronic structure are mutually consistent. We find, as expected, that the on-site Hubbard U correction is crucial to obtain the correct trends for various properties of these materials, but that quantitative predictions require the inclusion of the inter-site Hubbard V term. This capability allows us to carefully characterize the structural and electronic properties as well as provide accurate Li-intercalation voltages in remarkable agreement with experiments. Therefore, we show that DFT+ U + V is currently the most accurate compu-

tational framework not only for the selected olivine-type cathode materials [40, 45] but also for the spinel cathode materials considered here, motivating further studies of other families of Li-ion cathode materials.

The paper is organized as follows: in Sec. II we describe the computational method; in Sec. III we summarize the computational details of the study; in Sec. IV we present our findings for the structural, electronic, and electrochemical properties of $\text{Li}_x\text{Mn}_2\text{O}_4$ and $\text{Li}_x\text{Mn}_{1.5}\text{Ni}_{0.5}\text{O}_4$ ($x = 0$ and 1) using DFT, DFT+ U , and DFT+ U + V ; and in Sec. V we present the conclusions.

II. Computational method

In this section we briefly discuss the basics of the DFT+ U + V approach [36] and of the DFPT approach for computing Hubbard parameters [50, 51]. All equations in this subsection can be easily reduced to the DFT+ U case by setting $V = 0$. For the sake of simplicity, the formalism is presented in the framework of norm-conserving pseudopotentials in the collinear spin-polarized case. The generalization to the ultrasoft pseudopotentials and the projector augmented wave method can be found in Ref. [51]. Hartree atomic units are used.

A. DFT+ U + V

In DFT+ U + V , a correction term is added to the approximate DFT energy functional [36]:

$$E_{\text{DFT}+U+V} = E_{\text{DFT}} + E_{U+V}, \quad (1)$$

where E_{DFT} is the approximate DFT energy (constructed, e.g., using (semi-)local exchange-correlation functionals), and E_{U+V} contains the additional Hubbard term. At variance with the DFT+ U approach that contains only on-site interactions scaled by U , DFT+ $U+V$ contains also inter-site interactions between an atom and its surrounding ligands scaled by V . In the case of cathode materials studied here, the on-site U correction is needed for the Mn(3d) and Ni(3d) states, while the inter-site V correction is needed for Mn(3d)–O(2p) and Ni(3d)–O(2p) interactions [39]. We note that the inter-site V interactions for Mn(3d)–Ni(3d) couples are vanishing and hence these are neglected. In the simplified rotationally-invariant formulation [27], the extended Hubbard energy term reads:

$$E_{U+V} = \frac{1}{2} \sum_I \sum_{\sigma mm'} U^I (\delta_{mm'} - n_{mm'}^{II\sigma}) n_{m'm}^{II\sigma} - \frac{1}{2} \sum_I \sum_{J(J \neq I)}^* \sum_{\sigma mm'} V^{IJ} n_{mm'}^{IJ\sigma} n_{m'm}^{JI\sigma}, \quad (2)$$

where I and J are atomic site indices, m and m' are the magnetic quantum numbers associated with a specific angular momentum [$l = 2$ for Mn(3d) and Ni(3d), $l = 1$ for O(2p)], U^I and V^{IJ} are the effective on-site and inter-site Hubbard parameters, and the star in the sum denotes that for each atom I , the index J covers all its neighbors up to a given distance (or up to a given shell).

The generalized occupation matrices $n_{mm'}^{IJ\sigma}$ are computed by projecting the Kohn-Sham states on localized orbitals $\phi_m^I(\mathbf{r})$ of neighboring atoms:

$$n_{mm'}^{IJ\sigma} = \sum_{v,\mathbf{k}} f_{v,\mathbf{k}}^\sigma \langle \psi_{v,\mathbf{k}}^\sigma | \phi_{m'}^J \rangle \langle \phi_m^I | \psi_{v,\mathbf{k}}^\sigma \rangle, \quad (3)$$

where v and σ represent, respectively, the band and spin labels of the Kohn-Sham wavefunctions $\psi_{v,\mathbf{k}}^\sigma(\mathbf{r})$, \mathbf{k} indicate points in the first Brillouin zone, $f_{v,\mathbf{k}}^\sigma$ are the occupations of the Kohn-Sham states, and $\phi_m^I(\mathbf{r}) \equiv \phi_m^{\gamma(I)}(\mathbf{r} - \mathbf{R}_I)$ are localized orbitals centered on the I th atom of type $\gamma(I)$ at the position \mathbf{R}_I . It is convenient to establish a short-hand notation for the on-site occupation matrix: $n_{mm'}^{I\sigma} \equiv n_{mm',\mathbf{k}}^{II\sigma}$, which is used in the standard DFT+ U approach that corresponds to the first line of Eq. (2). Computing the values of U^I and V^{IJ} parameters is crucial to determine the degree of localization of 3d electrons on Mn and Ni sites and the degree of hybridization of these 3d electrons with 2p electrons centered on neighboring O sites. In the next subsection we discuss briefly how these Hubbard parameters can be computed using DFPT.

B. Calculation of Hubbard parameters

The values of Hubbard parameters are not known *a priori*, and hence often these values are adjusted em-

pirically such that the final results of simulations match some experimental properties of interest. This is fairly arbitrary, therefore, first-principles calculation of Hubbard parameters for any system at hand is essential and highly desirable. Hubbard U and V can be computed from a generalized piece-wise linearity condition imposed through linear-response theory [53] based on DFPT [50, 51]. Within this framework the Hubbard parameters are the elements of an effective interaction matrix computed as the difference between bare and screened inverse susceptibilities [53]:

$$U^I = (\chi_0^{-1} - \chi^{-1})_{II}, \quad (4)$$

$$V^{IJ} = (\chi_0^{-1} - \chi^{-1})_{IJ}, \quad (5)$$

where χ_0 and χ are the susceptibilities which measure the response of atomic occupations to shifts in the potential acting on individual Hubbard manifolds. In particular, χ is defined as $\chi_{IJ} = \sum_{m\sigma} (dn_{mm'}^{I\sigma}/d\alpha^J)$, where α^J is the strength of the perturbation of electronic occupations of the J th site. While χ is evaluated at self-consistency of the DFPT calculation, χ_0 (which has a similar definition as χ) is computed before the self-consistent readjustment of the Hartree and exchange-correlation potentials [50]. In DFPT, the response of the occupation matrix is computed in a primitive unit cell as:

$$\frac{dn_{mm'}^{I\sigma}}{d\alpha^J} = \frac{1}{N_{\mathbf{q}}} \sum_{\mathbf{q}} e^{i\mathbf{q} \cdot (\mathbf{R}_I - \mathbf{R}_{I'})} \Delta_{\mathbf{q}}^{s'} n_{mm'}^{s\sigma}, \quad (6)$$

where \mathbf{q} is the wavevector of the monochromatic perturbation, $N_{\mathbf{q}}$ is the total number of \mathbf{q} 's, $\Delta_{\mathbf{q}}^{s'} n_{mm'}^{s\sigma}$ is the lattice-periodic response of atomic occupations to a \mathbf{q} -specific monochromatic perturbation, $I \equiv (l, s)$ and $J \equiv (l', s')$ where s and s' are the atomic indices in unit cells while l and l' are the unit cell indices, \mathbf{R}_l and $\mathbf{R}_{l'}$ are the Bravais lattice vectors. The \mathbf{q} grid is chosen fine enough to make the resulting atomic perturbations effectively decoupled from their periodic replicas. We stress that the main advantage of using DFPT is that it does not require the usage of computationally expensive supercells contrary to the original linear-response formulation of Ref. [54]. It is crucial to recall that the values of the computed Hubbard parameters strongly depend on the type of Hubbard projector functions that are used in the DFT+ U and DFT+ $U+V$ approaches; this aspect is discussed in more detail in the next subsection.

C. Hubbard projectors

The Hubbard manifold $\{\phi_m^I(\mathbf{r})\}$ can be constructed using different types of projector functions (see e.g. Refs. [55, 56]). Here we consider atomic orbitals that

x	Method	HP	$\text{Li}_x\text{Mn}_2\text{O}_4$		$\text{Li}_x\text{Mn}_{1.5}\text{Ni}_{0.5}\text{O}_4$	
			Mn1	Mn2	Mn	Ni
1	PBEsol+ U	U	6.20	6.52	6.55	7.53
	PBEsol+ $U+V$	U	6.20	6.62	6.63	7.80
		V	0.56 – 0.78	0.74 – 0.79	0.73 – 0.75	0.65
0	PBEsol+ U	U	6.54	6.59	6.64	9.07
	PBEsol+ $U+V$	U	6.78	6.80	6.98	9.39
		V	0.84 – 0.89	0.85 – 0.87	0.90 – 0.94	0.86

TABLE I: Self-consistent Hubbard parameters (HP) in eV for $\text{Li}_x\text{Mn}_2\text{O}_4$ and $\text{Li}_x\text{Mn}_{1.5}\text{Ni}_{0.5}\text{O}_4$ at $x = 1$ and $x = 0$ computed using DFPT (PBEsol functional) in the basis of Löwdin-orthogonalized atomic orbitals as Hubbard projector functions.

are orthogonalized using the Löwdin method [57, 58]:

$$\phi_m^I(\mathbf{r}) = \sum_{Jm'} \left(\hat{O}^{-\frac{1}{2}} \right)_{m'm}^{JI} \varphi_{m'}^J(\mathbf{r}), \quad (7)$$

where $\varphi_m^I(\mathbf{r})$ are the nonorthogonalized atomic orbitals, \hat{O} is the orbital overlap matrix which is defined as $(\hat{O})_{m_1 m_2}^{IJ} = \langle \varphi_{m_1}^I | \varphi_{m_2}^J \rangle$, and $(\hat{O})_{m_1 m_2}^{IJ}$ is a matrix element of \hat{O} . This basis set better represents hybridizations of orbitals between neighboring sites, but especially it allows us to avoid counting Hubbard corrections twice in the interstitial regions between atoms. It is important to note that Löwdin-orthogonalized atomic orbitals are not truncated at some cutoff radius (at variance with other implementations, Refs. [59, 60]), which thus eliminates ambiguities due to the choice of such a cutoff radius [56, 61].

III. Computational details

All calculations are performed using the QUANTUM ESPRESSO distribution [62–64]. For LiMn_2O_4 , a supercell composed of 8 formula units (56 atoms) is used in order to model an AFM collinear magnetic ordering with a space group $Imma$, following Ref. [32]. This supercell is a pseudo-cubic cell that is built starting from an orthorhombic spinel structure [65]. The AFM ordering is chosen to be the lowest-energy one found in Ref. [32], and is shown in Fig. 1(a). Two types of Mn ions, labeled here as Mn1 and Mn2, correspond respectively to Mn^{3+} and Mn^{4+} that were observed experimentally. For $\text{LiMn}_{1.5}\text{Ni}_{0.5}\text{O}_4$, a supercell composed of 8 formula units (56 atoms) is also used in order to model a FiM collinear magnetic ordering [15, 20, 21] with a space group $Fd\bar{3}m$, and is shown in Fig. 1(b). We have checked that different cation orderings within $Fd\bar{3}m$ lead to the same electronic structure. The delithiated materials, Mn_2O_4 and $\text{Mn}_{1.5}\text{Ni}_{0.5}\text{O}_4$, are modelled using the same supercells and magnetic orderings as described above, and are constructed by simply removing all Li atoms. It is worth mentioning that Mn_2O_4 corresponds to the λ phase of

MnO_2 [12, 66].

For the xc functional we use a PBEsol [67] spin-polarized generalized-gradient approximation [68]. Pseudopotentials are those of the SSPP library v1.1 (precision) [69, 70]: `mn_pbesol_v1.5.uspp.F.UPF` (GBRV library v1.5 [71]), `0.pbesol-n-kjpaw_ps1.0.1.UPF` (Pslibrary v0.3.1 [72]), `ni_pbesol_v1.4.uspp.F.UPF` and `li_pbesol_v1.4.uspp.F.UPF` (GBRV library v1.4 [71]). For metallic ground states, we use the Marzari-Vanderbilt (MV) smearing [73] with a broadening parameter of 0.01 Ry. The crystal structure for all spin configurations is optimized at three levels of theory (PBEsol, PBEsol+ U , and PBEsol+ $U+V$) using the Broyden-Fletcher-Goldfarb-Shanno (BFGS) algorithm [74] with convergence thresholds of 10^{-6} Ry, 10^{-5} Ry/Bohr, and 0.5 KBar for the total energy, forces, and pressure, respectively. For structural optimizations, the \mathbf{k} -point sampling of the Brillouin zone uses a uniform Γ -centered $6 \times 6 \times 6$ mesh. Kohn-Sham wavefunctions and charge density are expanded in plane waves up to a kinetic-energy cutoff of 90 and 1080 Ry, respectively. Projected density of states (PDOS) is plotted using a Gaussian smearing with a broadening parameter of 10^{-3} Ry.

In order to compute the Li-intercalation voltages in cathode materials, it is necessary to compute the total energy of bulk Li; this is modelled using PBEsol and the *bcc* unit cell with one Li atom at the origin. The optimized lattice parameter is 3.436 Å, the Brillouin zone is sampled using the uniform Γ -centered $10 \times 10 \times 10$ \mathbf{k} -point mesh, and we use the MV smearing with a broadening of 0.02 Ry. The Kohn-Sham wavefunctions and charge density are expanded in plane waves up to a kinetic-energy cutoff of 65 and 780 Ry, respectively.

PBEsol+ U and PBEsol+ $U+V$ calculations are performed using the Löwdin-orthogonalized atomic orbitals as Hubbard projectors [56–58]. Hubbard U and V parameters are computed using DFPT [50, 51] as implemented in the HP code [75] which is part of QUANTUM ESPRESSO. It is worth noting that computationally expensive summations over empty states in perturbation theory are avoided thanks to the use of projectors on empty states manifolds (see e.g. Refs. [76, 77]). We have

used uniform Γ -centered \mathbf{k} - and \mathbf{q} -point meshes of size $4 \times 4 \times 4$ and $2 \times 2 \times 2$, respectively. Kohn-Sham wavefunctions and charge density are expanded in plane waves up to a kinetic-energy cutoff of 65 and 780 Ry, respectively, with an accuracy in the computed Hubbard parameters of ~ 0.01 eV. It is important to stress that we have used a self-consistent procedure for the calculation of U and V , as described in detail in Ref. [51], which consists of cyclic calculations containing structural optimizations and recalculations of Hubbard parameters for each new geometry. This procedure has proven to provide accurate results for various TM compounds [78–83]. The resulting Hubbard parameters are presented in Table I. It can be seen that the values of Hubbard U for Mn and Ni ions are sensitive to their oxidation state (OS) (see Sec. IV B), in line with previous studies for phospho-olivines [40, 45]. Hubbard V values show changes of only $\sim 0.1 - 0.2$ eV upon (de-)lithiation due to changes in the metal-ligand interatomic distances and electronic screening.

The data used to produce the results of this paper are available in the Materials Cloud Archive [84].

IV. Results and discussion

A. Structural properties

Tables II and III compare the lattice parameters and cell volumes for $\text{Li}_x\text{Mn}_2\text{O}_4$ and $\text{Li}_x\text{Mn}_{1.5}\text{Ni}_{0.5}\text{O}_4$ ($x = 0$ and 1) optimized using PBEsol, PBEsol+ U , and PBEsol+ $U+V$ as well as the experimental values [8, 11, 85]. For LiMn_2O_4 , PBEsol underestimates the cell volume by 7.7%, while PBEsol+ U overestimates it by 2.4%, and PBEsol+ $U+V$ provides the most accurate prediction with a small overestimation of 1.2%. For Mn_2O_4 , the trend is different. Namely, PBEsol predicts the cell volume which is in closest agreement with experimental values and is underestimated by 2.7%, while PBEsol+ U overestimates the cell volume by 6.6%, and PBEsol+ $U+V$ also overestimates it but by a smaller margin of 3.9%.

In the case of partial substitution of Ni for Mn, the trends are the same but more pronounced. For $\text{LiMn}_{1.5}\text{Ni}_{0.5}\text{O}_4$, PBEsol underestimates the cell volume by 3.2%, while PBEsol+ U overestimates it by 4.1%, and PBEsol+ $U+V$ again provides the most accurate prediction with an overestimation of 2.7% (which is about as twice large as the case of LiMn_2O_4). For $\text{Mn}_{1.5}\text{Ni}_{0.5}\text{O}_4$, again PBEsol provides remarkable agreement with the experimental cell volume with an underestimation of only 1.0%, while both PBEsol+ U and PBEsol+ $U+V$ show quite a large overestimation by 6.5% and 6.2%, respectively. Importantly, only using PBEsol+ U and PBEsol+ $U+V$ we find that the cell volume is decreased by partially substituting Ni for Mn in LiMn_2O_4 in agreement with experiments, while PBEsol incorrectly shows the opposite trend. In the fully delithiated material, conversely, all levels of theory are consistent with experi-

Method	LP	LiMn_2O_4	Mn_2O_4
PBEsol	a (Å)	8.06	7.99
	b (Å)	8.06	7.99
	c (Å)	8.08	7.98
	V (Å ³)	525.0	509.6
PBEsol+ U	a (Å)	8.18	8.24
	b (Å)	8.18	8.24
	c (Å)	8.72	8.23
	V (Å ³)	582.7	558.2
PBEsol+ $U+V$	a (Å)	8.13	8.17
	b (Å)	8.13	8.17
	c (Å)	8.71	8.16
	V (Å ³)	575.5	544.2
Expt. [8, 11, 85]	a (Å)	8.11	8.06
	b (Å)	8.11	8.06
	c (Å)	8.65	8.06
	V (Å ³)	568.9	523.6

TABLE II: Pseudo-cubic lattice parameters (a , b , and c) and cell volume (V) of $\text{Li}_x\text{Mn}_2\text{O}_4$ at $x = 1$ and $x = 0$.

Method	LP	$\text{LiMn}_{1.5}\text{Ni}_{0.5}\text{O}_4$	$\text{Mn}_{1.5}\text{Ni}_{0.5}\text{O}_4$
PBEsol	a (Å)	8.08	7.97
	V (Å ³)	528.1	506.8
PBEsol+ U	a (Å)	8.28	8.17
	V (Å ³)	567.8	545.2
PBEsol+ $U+V$	a (Å)	8.24	8.16
	V (Å ³)	560.0	543.6
Expt. [18, 86]	a (Å)	8.17	8.00
	V (Å ³)	545.3	512.0

TABLE III: Cubic lattice parameter (a) and cell volume (V) of $\text{Li}_x\text{Mn}_{1.5}\text{Ni}_{0.5}\text{O}_4$ at $x = 1$ and $x = 0$.

ments and show that the cell volume decreases upon the partial substitution of Ni for Mn.

In summary, while PBEsol+ $U+V$ predicts the crystal structure of fully lithiated spinel cathodes most accurately, it is still less accurate than PBEsol for the fully delithiated structures, in line with similar findings for phospho-olivines [40, 45]. Relatively large overestimations of the cell volume in the delithiated structures are mainly driven by the large on-site Hubbard U correction, while inter-site V corrections counteract it and reduce this effect. The effect of inter-site Hubbard V interactions, therefore, is an essential correction on top of PBEsol+ U to provide an improved description of the structural properties of the spinel cathode materials.

B. Löwdin occupations, magnetic moments, and oxidation state

As mentioned in the introduction, in LiMn_2O_4 , Mn exists in two OS, namely Mn^{3+} and Mn^{4+} , in an equal 1 : 1 ratio. Upon delithiation, each Mn^{3+} ion loses one electron and thus oxidizes to Mn^{4+} , and as a result in Mn_2O_4 all Mn ions are in the +4 OS [12]. On the other hand, in $\text{LiMn}_{1.5}\text{Ni}_{0.5}\text{O}_4$ all Mn ions are in the +4 OS while all Ni ions are in the +2 OS (the ratio of Ni to Mn is 1 : 3). Upon delithiation, each Ni ion loses two electrons and as a consequence they all oxidize from Ni^{2+} to Ni^{4+} , while the Mn^{4+} ions remain unchanged [17].

Theoretical determination of the OS of TM ions based on (Hubbard-corrected) PBEsol calculations is not a trivial task, and can be carried out using different methods (see e.g. Ref. [45] for a brief review). In particular, the atomic occupations—that are computed by projecting the Kohn-Sham wavefunctions on a certain type of atom-centered localized orbitals (and thus are not uniquely defined)—are often used to determine the OS, but this approach can lead to the wrong conclusion due to the so-called negative-feedback charge regulation mechanism [88, 89]. Another popular proxy that is commonly used to determine the OS of TM ions are magnetic moments. However, magnetic moments are also not uniquely defined: they are either computed by integrating the magnetization density inside the spheres centered on atoms (and hence depend on the cutoff radius [90]) or computed via difference of the spin-up and spin-down components of the Kohn-Sham wavefunctions projected on atom-centered localized functions (and hence depend on the specific type of these localized functions). Additionally, a given OS can have multiple spin configurations (e.g., high or low spin) which have distinct magnetic moments. Since none of these methods are very reliable [45], we chose to use the projection-based method proposed by Sit and coworkers that uses eigenvalues of the atomic occupation matrix to determine the OS of TM ions [87].

Table IV presents the spin-resolved eigenvalues of the atomic occupations matrices, Löwdin occupations, magnetic moments, and OSs computed using PBEsol, PBEsol+ U , and PBEsol+ $U+V$ for all materials studied here. According to Ref. [87], in order to determine the OS, we only need to count the eigenvalues that are close to 1.0, and all others (distinctly lower than 1) must be disregarded since they describe electrons that are shared between TM ions and ligands – here, the O-2 p states – and hence do not belong exclusively to the former. Moreover, for the sake of clarity, in Fig. 2 we show how many electrons must be in the 3 d shells of TM ions in order to correspond to Mn^{3+} , Mn^{4+} , Ni^{2+} , and Ni^{4+} . We can see from Table IV, that only PBEsol+ U and PBEsol+ $U+V$ correctly predict the OS of Mn and Ni ions in the fully lithiated and delithiated spinel materials, while PBEsol fails and incorrectly predicts the +4 OS for Mn1 and Ni in the lithiated compounds. This failure of PBEsol is due to the overdelocalization of Mn-3 d

and Ni-3 d states originating from self-interaction errors inherent to local and semi-local xc functionals [91, 92]. These errors are successfully alleviated thanks to Hubbard U and V corrections [39, 93, 94]. Therefore, both within PBEsol+ U and PBEsol+ $U+V$ we find Mn^{4+} and high-spin Mn^{3+} in LiMn_2O_4 , and only Mn^{4+} in Mn_2O_4 ; and in $\text{LiMn}_{1.5}\text{Ni}_{0.5}\text{O}_4$ we find Mn^{4+} and Ni^{2+} , while in $\text{Mn}_{1.5}\text{Ni}_{0.5}\text{O}_4$ we find Mn^{4+} and low-spin Ni^{4+} .

It is useful here to comment on Löwdin occupations. Indeed, due to the negative-feedback charge regulation mechanism [88, 89], in $\text{Li}_x\text{Mn}_2\text{O}_4$ we find too small changes in the Löwdin occupations upon delithiation (from $x = 1$ to $x = 0$); more specifically, within PBEsol+ $U+V$ the occupations for Mn1 ions change only from 5.05 to 5.02, while the nominal occupations change from 4.00 (Mn^{3+}) to 3.00 (Mn^{4+}). Even though the absolute values of Löwdin occupations are not very reliable due to their strong dependence on the type of atom-centered localized functions on which one projects the Kohn-Sham wavefunctions, we highlight here that the lack of the correct change in the Löwdin occupations upon delithiation makes it impossible to determine the OS, as previously mentioned. Similar observations can be made for the Löwdin occupations of Ni ions in $\text{Li}_x\text{Mn}_{1.5}\text{Ni}_{0.5}\text{O}_4$ upon delithiation. Namely, within PBEsol+ $U+V$ the occupations for Ni ions change only from 8.24 to 8.13, while the nominal occupations change from 8.00 (Ni^{2+}) to 6.00 (Ni^{4+}). Similar trends are observed also within PBEsol and PBEsol+ U confirming that Löwdin occupations are not a good proxy for determining the OS.

Lastly, let us analyze the magnetic moments. Within PBEsol+ $U+V$ for $\text{Li}_x\text{Mn}_2\text{O}_4$, the magnetic moments for Mn1 ions change from 3.95 to 3.33 μ_B upon delithiation, while the nominal magnetic moments change from 4.00 (Mn^{3+}) to 3.00 μ_B (Mn^{4+}). Therefore, even though the absolute values of magnetic moments for Mn ions do not match precisely the nominal ones (and this is correct due to orbital hybridization effects in the crystal compared to an isolated atom in an idealized undistorted octahedral complex, see Fig. 2), it is quite straightforward to make correct attributions of OSs to Mn1 ions to be Mn^{3+} and Mn^{4+} in LiMn_2O_4 and Mn_2O_4 , respectively. However, such an analysis is much less clear in the case of $\text{Li}_x\text{Mn}_{1.5}\text{Ni}_{0.5}\text{O}_4$. Indeed, within PBEsol+ $U+V$ the magnetic moments of Ni ions change from -1.71 to 1.06 μ_B upon delithiation, while the nominal magnetic moments change from -2.00 (Ni^{2+}) to 0.00 μ_B (Ni^{4+}). Neither PBEsol nor PBEsol+ U are able to show changes in magnetic moments for Ni ions similar to the nominal ones. This is due to the fact that the partial occupancy of the “formally empty” (but hybridized in practice) spin-up and spin-down channels of Ni ions are very sensitive to the Hubbard corrections [46]. Therefore, it turns out that the magnetic moments are not always a reliable proxy for determining the OS of TM ions. Finally, for the sake of completeness, we remark that at all levels of theory the total net magnetization is exactly

Material	Method	Type	λ_1^\uparrow	λ_2^\uparrow	λ_3^\uparrow	λ_4^\uparrow	λ_5^\uparrow	λ_1^\downarrow	λ_2^\downarrow	λ_3^\downarrow	λ_4^\downarrow	λ_5^\downarrow	n	m (μ_B)	OS
LiMn_2O_4	PBEsol	Mn1	0.47	0.49	0.99	0.99	0.99	0.18	0.24	0.27	0.33	0.33	5.25	2.58	+4
		Mn2	0.44	0.44	0.98	0.99	0.99	0.15	0.26	0.31	0.35	0.38	5.28	2.39	+4
	PBEsol+ U	Mn1	0.56	0.99	1.00	1.00	1.00	0.04	0.04	0.06	0.14	0.22	5.02	4.05	+3
		Mn2	0.64	0.65	0.99	1.00	1.00	0.06	0.07	0.07	0.24	0.27	4.98	3.57	+4
	PBEsol+ $U+V$	Mn1	0.52	0.99	1.00	1.00	1.00	0.04	0.05	0.07	0.15	0.24	5.05	3.95	+3
		Mn2	0.59	0.60	1.00	1.00	1.00	0.08	0.08	0.09	0.27	0.30	5.00	3.37	+4
	Nominal	Mn1	0.00	1.00	1.00	1.00	1.00	0.00	0.00	0.00	0.00	0.00	4.00	4.00	+3
		Mn2	0.00	0.00	1.00	1.00	1.00	0.00	0.00	0.00	0.00	0.00	3.00	3.00	+4
Mn_2O_4	PBEsol	Mn1	0.49	0.50	0.98	0.98	0.99	0.15	0.16	0.20	0.36	0.37	5.16	2.71	+4
		Mn2	0.49	0.51	0.98	0.98	0.99	0.15	0.16	0.19	0.34	0.37	5.16	2.75	+4
	PBEsol+ U	Mn1	0.64	0.65	1.00	1.00	1.00	0.06	0.06	0.08	0.26	0.26	4.99	3.55	+4
		Mn2	0.65	0.67	0.99	0.99	1.00	0.06	0.06	0.08	0.24	0.25	4.99	3.63	+4
	PBEsol+ $U+V$	Mn1	0.59	0.60	1.00	1.00	1.00	0.07	0.07	0.10	0.30	0.30	5.02	3.33	+4
		Mn2	0.60	0.62	0.99	1.00	1.00	0.07	0.07	0.10	0.28	0.29	5.01	3.40	+4
	Nominal	Mn1	0.00	0.00	1.00	1.00	1.00	0.00	0.00	0.00	0.00	0.00	3.00	3.00	+4
		Mn2	0.00	0.00	1.00	1.00	1.00	0.00	0.00	0.00	0.00	0.00	3.00	3.00	+4
$\text{LiMn}_{1.5}\text{Ni}_{0.5}\text{O}_4$	PBEsol	Mn	0.48	0.48	0.99	0.99	0.99	0.15	0.17	0.26	0.34	0.34	5.18	2.68	+4
		Ni	0.35	0.35	0.97	0.97	0.97	0.87	0.87	0.99	0.99	0.99	8.29	-1.08	+4
	PBEsol+ U	Mn	0.64	0.66	1.00	1.00	1.00	0.06	0.06	0.08	0.23	0.26	4.98	3.61	+4
		Ni	0.14	0.14	0.98	0.99	0.99	0.99	0.99	1.00	1.00	1.00	8.21	-1.74	+2
	PBEsol+ $U+V$	Mn	0.60	0.62	1.00	1.00	1.00	0.07	0.07	0.10	0.27	0.29	5.00	3.41	+4
		Ni	0.15	0.15	0.99	0.99	0.99	0.99	0.99	0.99	1.00	1.00	8.24	-1.71	+2
	Nominal	Mn	0.00	0.00	1.00	1.00	1.00	0.00	0.00	0.00	0.00	0.00	3.00	3.00	+4
		Ni	0.00	0.00	1.00	1.00	1.00	1.00	1.00	1.00	1.00	1.00	8.00	-2.00	+2
$\text{Mn}_{1.5}\text{Ni}_{0.5}\text{O}_4$	PBEsol	Mn	0.51	0.51	0.97	0.99	0.99	0.13	0.15	0.19	0.35	0.36	5.14	2.79	+4
		Ni	0.59	0.59	0.99	0.99	0.99	0.52	0.52	0.98	0.98	0.99	8.15	0.16	+4
	PBEsol+ U	Mn	0.66	0.67	0.99	1.00	1.00	0.05	0.06	0.08	0.24	0.25	4.99	3.64	+4
		Ni	0.42	0.42	0.99	0.99	0.99	0.68	0.68	1.00	1.00	1.00	8.16	-0.53	+4
	PBEsol+ $U+V$	Mn	0.62	0.63	0.99	1.00	1.00	0.06	0.07	0.09	0.27	0.28	5.00	3.47	+4
		Ni	0.81	0.81	1.00	1.00	1.00	0.28	0.28	1.00	1.00	1.00	8.13	1.06	+4
	Nominal	Mn	0.00	0.00	1.00	1.00	1.00	0.00	0.00	0.00	0.00	0.00	3.00	3.00	+4
		Ni	0.00	0.00	1.00	1.00	1.00	0.00	0.00	1.00	1.00	1.00	6.00	0.00	+4

TABLE IV: Löwdin population analysis data for the $3d$ shell of Mn and Ni ions in $\text{Li}_x\text{Mn}_2\text{O}_4$ and $\text{LiMn}_{1.5}\text{Ni}_{0.5}\text{O}_4$ at $x = 0$ and $x = 1$ computed using three approaches: PBEsol, PBEsol+ U , and PBEsol+ $U+V$. We compare these values with the expectations from using the nominal valence of the TM ions. This table shows the eigenvalues of the site-diagonal occupation matrix for the spin-up (λ_i^\uparrow , $i = \overline{1, 5}$) and spin-down (λ_i^\downarrow , $i = \overline{1, 5}$) channels, Löwdin occupations $n = \sum_i (\lambda_i^\uparrow + \lambda_i^\downarrow)$, magnetic moments $m = \sum_i (\lambda_i^\uparrow - \lambda_i^\downarrow)$, and the oxidation state (OS). In LiMn_2O_4 and Mn_2O_4 , which are both AFM, the magnetic moments of Mn1 and Mn2 have both positive and negative values (see Fig. 1(a)), and here we report only the positive values. The eigenvalues are written in the ascending order (from left to right) for each spin channel. The eigenvalues written in bold correspond to fully occupied states and thus are taken into account when determining the OS according to Ref. [87].

zero for LiMn_2O_4 and Mn_2O_4 , while it is 3.5 and 4.5 μ_B per formula unit for $\text{LiMn}_{1.5}\text{Ni}_{0.5}\text{O}_4$ and $\text{Mn}_{1.5}\text{Ni}_{0.5}\text{O}_4$, respectively, in agreement with theoretical nominal net magnetizations [15, 21].

C. Band gaps

From experimental observations it is known that LiMn_2O_4 is insulating with a band gap of ~ 1.2 eV [95]; however, we are not aware of any experimental reports for Mn_2O_4 (λ - MnO_2). Table V summarizes the

computed band gaps for these two compounds using PBEsol, PBEsol+ U , and PBEsol+ $U+V$. It can be seen for LiMn_2O_4 that PBEsol predicts a metallic ground state, PBEsol+ U underestimated the gap by 39%, while PBEsol+ $U+V$ predicts a band gap of 1.19 eV in excellent agreement with the experimental value of Ref. [95] and in good agreement with the value of 1.1 eV computed using the PBE0r hybrid functional [34]. This agrees with the previous findings that PBEsol+ U often improves the band gaps compared to PBEsol [82, 83], while PBEsol+ $U+V$ outperforms PBEsol+ U in terms of accuracy for band gaps [43, 44]. For Mn_2O_4 , PBEsol pre-

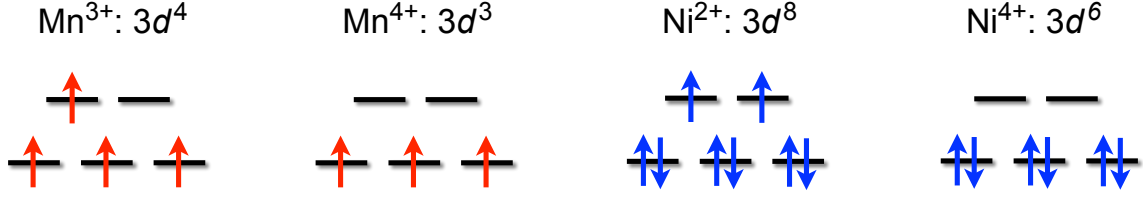


FIG. 2: Nominal occupations of the $3d$ manifold of Mn and Ni atoms (not hybridized with ligands) in an undistorted octahedral complex with different oxidation states (O_h point group). The t_{2g} (three lower) and e_g (two higher) levels are indicated with black horizontal lines and are nondegenerate due to the crystal-field splitting; up and down arrows correspond to spin-up and spin-down electrons, respectively.

Method	LiMn ₂ O ₄	Mn ₂ O ₄
PBEsol	0.00	1.05
PBEsol+ U	0.73	1.44
PBEsol+ $U+V$	1.19	2.05
PBE0r [34]	1.1	2.2
Expt. [95]	1.2	

TABLE V: Band gaps (in eV) of Li _{x} Mn₂O₄ at $x = 1$ and $x = 0$.

Method	LiMn _{1.5} Ni _{0.5} O ₄	Mn _{1.5} Ni _{0.5} O ₄
PBEsol	0.00	0.37
PBEsol+ U	0.33	0.62
PBEsol+ $U+V$	0.76	0.42

TABLE VI: Band gaps (in eV) of Li _{x} Mn_{1.5}Ni_{0.5}O₄ at $x = 1$ and $x = 0$.

dicts the smallest band gap, PBEsol+ $U+V$ the largest, while PBEsol+ U provides the band gap in between. It is worth noting that the PBEsol+ $U+V$ value of 2.05 eV is close to the band gap value of 2.2 eV that was computed using PBE0r [34], thus suggesting that these values should be reliable.

Unfortunately, for LiMn_{1.5}Ni_{0.5}O₄ and Mn_{1.5}Ni_{0.5}O₄ there are no experimental data for the band gaps, to the best of our knowledge; however, the work of Ref. [96] states that LiMn_{1.5}Ni_{0.5}O₄ has an insulating ground state. Table VI presents the band gaps for these two compounds computed using PBEsol, PBEsol+ U , and PBEsol+ $U+V$. Like in the case of LiMn₂O₄, for LiMn_{1.5}Ni_{0.5}O₄ PBEsol predicts a metallic ground state, while the fully delithiated counterpart (i.e. Mn_{1.5}Ni_{0.5}O₄) has some finite but very small band gap of 0.37 eV. On the other hand, PBEsol+ U opens a gap in LiMn_{1.5}Ni_{0.5}O₄, while PBEsol+ $U+V$ further enhances it, similar to the case of LiMn₂O₄. In Mn_{1.5}Ni_{0.5}O₄, conversely, while PBEsol+ U increases the gap compared to PBEsol, PBEsol+ $U+V$ reduces it back and falls in-between the PBEsol and PBEsol+ U values. Therefore, we believe that the PBEsol+ $U+V$ band gaps of 0.76 and 0.42 eV for LiMn_{1.5}Ni_{0.5}O₄ and Mn_{1.5}Ni_{0.5}O₄, respectively, are the most reliable ones and should be used for comparisons in the future computational and experimental works.

D. Projected density of states

Spin-resolved projected density of states (PDOS) for all materials studied here computed using PBEsol, PBEsol+ U , and PBEsol+ $U+V$ are shown in Fig. 3. As was pointed out in this and previous theoretical works [7, 28–33], PBEsol is unable to distinguish between Mn³⁺ and Mn⁴⁺ ions in LiMn₂O₄ due to self-interaction errors leading to the overdelocalization of Mn- $3d$ states. This can be seen in Fig. 3(a), where both types of Mn ions show nearly identical PDOS across the entire energy range, and a metallic solution is found. Adding the Hubbard U correction to the Mn- $3d$ states allows them to localize and a clear energy separation between these Mn1- $3d$ (Mn³⁺) and Mn2- $3d$ (Mn⁴⁺) states can be seen, resulting in an insulating ground state. Adding the Hubbard V correction on top only leads to minor changes in the PDOS, consistently with the findings for other TM oxides [43, 44]. Overall, the Hubbard U and V corrections lead to a PDOS where the valence band maximum (VBM) is dominated by O- $2p$ states that are slightly hybridized with Mn³⁺- $3d$ states, while the conduction band minimum (CBM) consists of strongly mixed O- $2p$ and Mn⁴⁺- $3d$ states. Overall, the computed PDOS agrees well with the one from the previous PBEsol+ U works [28, 29, 32]. In Mn₂O₄, the PDOS for Mn1- $3d$ and Mn2- $3d$ states are nearly identical as both correspond to Mn⁴⁺. Within PBEsol, the character of the VBM shows a strong mixing of O- $2p$ and Mn⁴⁺- $3d$ states and the character of the CBM is predominantly Mn⁴⁺- $3d$. In contrast, within PBEsol+ U and PBEsol+ $U+V$ the character of the VBM is purely O- $2p$, while that of the CBM is predominantly O- $2p$ with a rather strong mixing with the Mn⁴⁺- $3d$ states. Therefore, we find that the inclu-

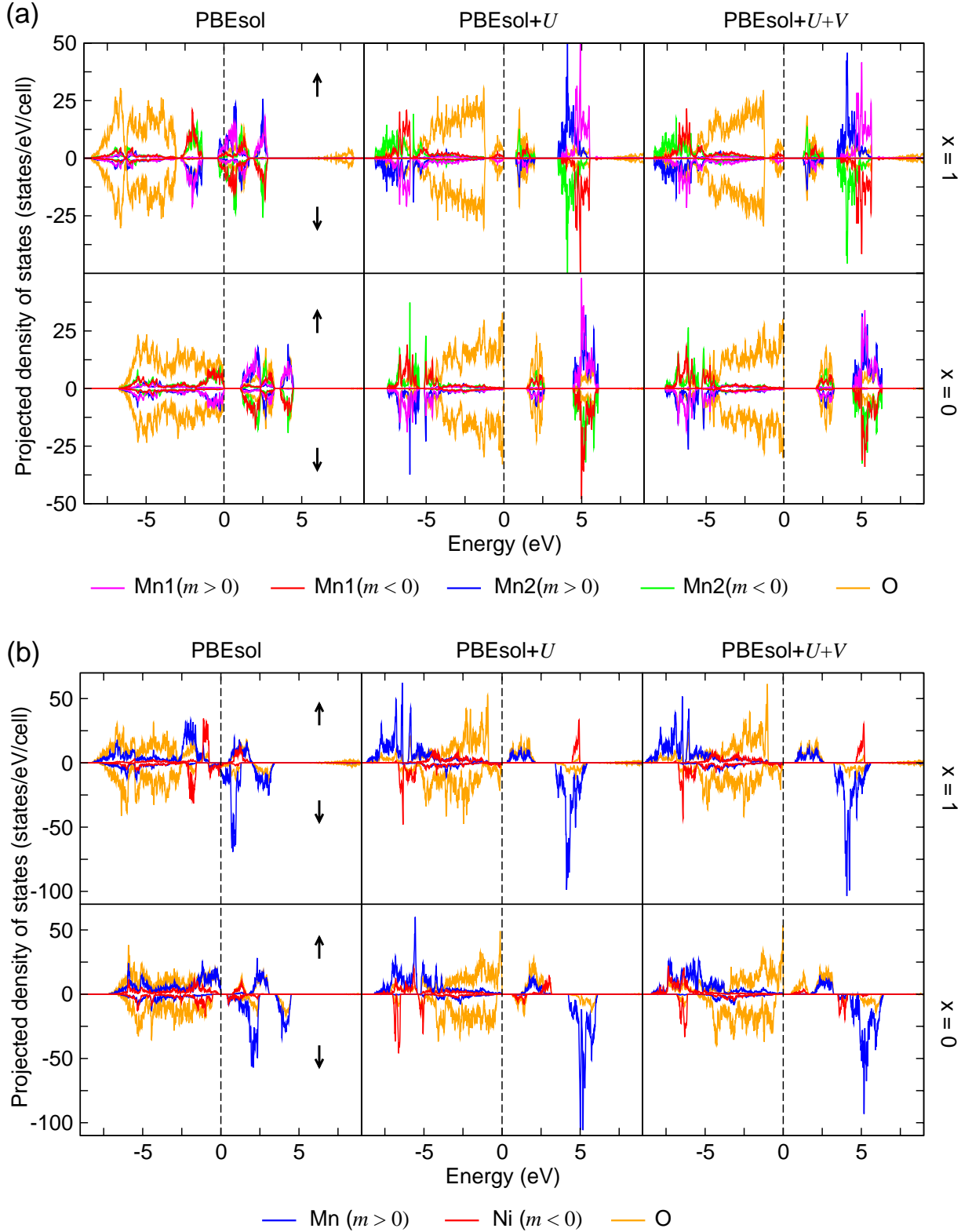


FIG. 3: Spin-polarized projected density of states of (a) $\text{Li}_x\text{Mn}_2\text{O}_4$ and (b) $\text{Li}_x\text{Mn}_{1.5}\text{Ni}_{0.5}\text{O}_4$ at $x = 1$ and $x = 0$ computed using PBEsol, PBEsol+ U , and PBEsol+ $U+V$. The zero of energy corresponds to the top of the valence bands in the case of insulating ground states or the Fermi level in the case of metallic ground states. The upper and lower parts of each panel correspond to the spin-up and spin-down channels, respectively. The sign of the magnetic moment m is highlighted for TM elements.

sion of the Hubbard corrections dramatically changes the PDOS of these two compounds.

In the case of $\text{LiMn}_{1.5}\text{Ni}_{0.5}\text{O}_4$ within PBEsol, both $\text{Mn}^{4+}-3d$ and $\text{Ni}^{2+}-3d$ states cross the Fermi level and hence are responsible for the metallicity of this material, thus contradicting to experiments. The addition of the Hubbard U and V corrections opens a gap: the character of the VBM is $\text{O}-2p$ while that of the CBM is strongly mixed between $\text{O}-2p$ and $\text{Mn}^{4+}-3d$ states. In contrast, in $\text{Mn}_{1.5}\text{Ni}_{0.5}\text{O}_4$ PBEsol opens a gap, with the character of the VBM being a mixture of $\text{Mn}^{4+}-3d$ and $\text{O}-2p$ states, while that of the CBM is a mixture of $\text{Mn}^{4+}-3d$ and $\text{Ni}^{4+}-3d$ states. Interestingly, PBEsol+ U and PBEsol+ $U+V$ give somewhat different PDOS for $\text{Mn}_{1.5}\text{Ni}_{0.5}\text{O}_4$, which is mainly due to the $\text{Ni}^{4+}-3d$ states. While in both cases the character of the VBM is purely $\text{O}-2p$, that of the CBM is $\text{O}-2p$ mixed with the $\text{Ni}^{4+}-3d$ states and both appearing either in the spin-down (PBEsol+ U) or spin-up channel (PBEsol+ $U+V$). As was pointed out in Sec. IV B, this is driven by the sensitivity of the $\text{Ni}^{4+}-3d$ electron distribution in the spin-up and spin-down channels to the Hubbard corrections. In order to gain more insight into the PDOS for $\text{Mn}_{1.5}\text{Ni}_{0.5}\text{O}_4$, it would be desirable to perform calculations using e.g. hybrid functionals or other methods of similar accuracy, ideally accompanied with photoemission experiments.

E. Voltages

The topotactic Li-intercalation voltages can be computed using the fundamental thermodynamic definition [40, 45, 97]:

$$\Phi = -\frac{E(\text{Li}_{x_2}\text{S}) - E(\text{Li}_{x_1}\text{S}) - (x_2 - x_1)E(\text{Li})}{(x_2 - x_1)e}, \quad (8)$$

where S is introduced for the sake of shorthand notation and it denotes Mn_2O_4 for $\text{Li}_x\text{Mn}_2\text{O}_4$, and $\text{Mn}_{1.5}\text{Ni}_{0.5}\text{O}_4$ for $\text{Li}_x\text{Mn}_{1.5}\text{Ni}_{0.5}\text{O}_4$. Here, Φ is the voltage, e is the electronic charge, x_1 and x_2 are the concentrations of Li, and E is the total energy per formula unit. It is important to remark that $E(\text{Li})$ is the total energy of bulk Li computed at the level of standard DFT (PBEsol functional) while $E(\text{Li}_{x_1}\text{S})$ and $E(\text{Li}_{x_2}\text{S})$ are computed using three functionals considered in this work: PBEsol, PBEsol+ U , and PBEsol+ $U+V$ (U and V are computed self-consistently individually for each structure) [40, 45]. If there are several plateaus in the voltage profile as a function of the Li concentration, it is possible to compute these by selecting corresponding x_1 and x_2 values in Eq. (8). Here we compute the average voltage in the whole range of Li concentrations and thus take $x_1 = 0$ and $x_2 = 1$. We also remark that the voltage can be computed at a low and high state of charge [98]. It is worth noting that the entropic and pressure-volume effects are neglected since these are not significant when computing the average Li-intercalation voltages [99].

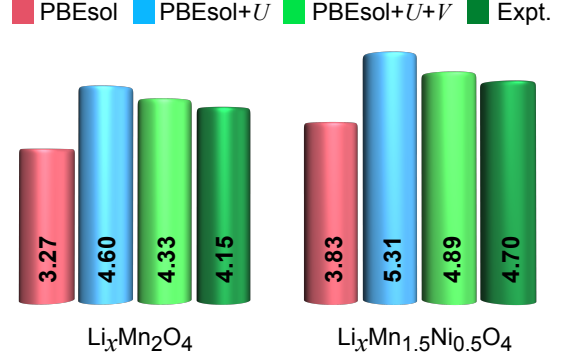


FIG. 4: Voltages versus Li/Li^+ (in V) for $\text{Li}_x\text{Mn}_2\text{O}_4$ and $\text{Li}_x\text{Mn}_{1.5}\text{Ni}_{0.5}\text{O}_4$ for $0 < x < 1$ computed using PBEsol, PBEsol+ U , and PBEsol+ $U+V$. The experimental data is from Refs. [5, 6, 100].

Figure 4 shows the comparison of average voltages versus Li/Li^+ for $0 < x < 1$ computed using PBEsol, PBEsol+ U , and PBEsol+ $U+V$ and compared with experimental ones from Refs. [5, 6, 100] (see also Ref. [7]). The observed trends are the same as for phospholivines [40, 45]. Namely, PBEsol underestimates the voltages by about 20%, while PBEsol+ U overestimates them by about 12%, and PBEsol+ $U+V$ provides the most accurate prediction of the voltages with an overestimation of about 4% (~ 0.2 V) compared to experiments. We want to stress that this is a remarkable result since here we used a fully first-principles framework with Hubbard parameters being computed from linear response and not empirically calibrated as is commonly done. The remaining discrepancies between the PBEsol+ $U+V$ and experimental voltages could be attributed in part to finite-temperature effects that have been neglected in this study, but further studies in this direction are needed.

V. Conclusions

We have presented a fully first-principles investigation of the structural, electronic, magnetic, and electrochemical properties of two prototypical spinel cathode materials – $\text{Li}_x\text{Mn}_2\text{O}_4$ and $\text{Li}_x\text{Mn}_{1.5}\text{Ni}_{0.5}\text{O}_4$ ($x = 0$ and $x = 1$) – using PBEsol, PBEsol+ U , and PBEsol+ $U+V$. The on-site U and inter-site V Hubbard parameters are computed self-consistently fully from first-principles using density-functional perturbation theory, hence avoiding any empiricism. We have shown that while the on-site U correction is crucial to reproduce the correct trends in the electronic-structure properties of these materials, the inter-site V is decisive for quantitatively accurate predictions of these. In particular, the Li-intercalation voltages are most accurate at the PBEsol+ $U+V$ level, with a deviation of about 4% (~ 0.2 V) from experiments. Lattice parameters, cell volumes, and band gaps are more accu-

rately predicted within PBEsol+ U + V than PBEsol+ U , underlining again the importance of inter-site Hubbard corrections due to significant metal-ligand hybridization in these materials. We have also shown that Löwdin occupations and magnetic moments are not reliable proxies for determining the oxidation state of transition-metal ions, while the approach of Sit and coworkers [87] is very robust in spinel materials, in analogy with phospho-olivines [45]. This allowed us to correctly identify the presence of Mn^{3+} and Mn^{4+} ions in LiMn_2O_4 , Mn^{4+} in Mn_2O_4 , Mn^{4+} and Ni^{2+} in $\text{LiMn}_{1.5}\text{Ni}_{0.5}\text{O}_4$, and Mn^{4+} and Ni^{4+} in $\text{Mn}_{1.5}\text{Ni}_{0.5}\text{O}_4$. This work, therefore, paves the way for accurate future studies of other families of Li-ion cathode materials using extended DFT+ U + V functionals.

Acknowledgements

This research was supported by the NCCR MARVEL, a National Centre of Competence in Research, funded by the Swiss National Science Foundation (grant number 205602). For the purpose of Open Access, a CC BY pub-

lic copyright licence is applied to any Author Accepted Manuscript (AAM) version arising from this submission. Computer time was provided by the Swiss National Supercomputing Centre (CSCS) under project No. s1073.

Author Contributions

Author contributions include conceptualization, I.T. and N.M.; methodology, I.T. and N.M.; software, I.T.; validation, I.T.; formal analysis, I.T., M.K., N.M.; investigation, I.T., M.K., N.M.; resources, I.T. and N.M.; data curation, I.T., M.K., N.M.; writing—original draft preparation, I.T.; writing—review and editing, I.T., M.K., N.M.; visualization, I.T. and M.K.; supervision, N.M.; project administration, I.T. and N.M.; funding acquisition, N.M. All authors have read and agreed to the published version of the manuscript.

Conflicts of interest

There are no conflicts to declare.

-
- [1] D. Larcher and J. Tarascon, Towards greener and more sustainable batteries for electrochemical energy storage, *Nat. Chem.* **7**, 19 (2014).
 - [2] B. Kang and G. Ceder, Battery materials for ultrafast charging and discharging, *Nature* **458**, 190 (2009).
 - [3] M. Thackeray, W. David, P. Bruce, and J. Goodenough, *Mater. Res. Bull.* **18**, 461 (1983).
 - [4] Y. Huang, Y. Dong, S. Li, J. Lee, C. Wang, Z. Zhu, W. Xue, Y. Li, and J. Li, Lithium Manganese Spinel Cathodes for Lithium-Ion Batteries, *Adv. Energy Mater.* **11**, 2000997 (2021).
 - [5] T. Ohzuku and A. Ueda, *Solid State Ionics* **69**, 201 (1994).
 - [6] J. Barker, K. West, Y. Saidi, R. Pynenburg, B. Zachau-Christiansen, and R. Koksang, Kinetics and thermodynamics of the lithium insertion reaction in spinel phase $\text{Li}_x\text{Mn}_2\text{O}_4$, *J. Power Sources* **54**, 475 (1995).
 - [7] F. Zhou, M. Cococcioni, C. Marianetti, D. Morgan, and G. Ceder, First-principles prediction of redox potentials in transition-metal compounds with LDA+ U , *Phys. Rev. B* **70**, 235121 (2004).
 - [8] R. Kanno, A. Kondo, M. Yonemura, R. Gover, Y. Kawamoto, M. Tabuchi, T. Kamiyama, F. Izumi, C. Masquelier, and G. Rousse, *J. Power Sources* **81-82**, 542 (1999).
 - [9] A. Yamada and M. Tanaka, *Mater. Res. Bull.* **30**, 715 (1995).
 - [10] J. Rodriguez-Carvajal, G. Rousse, C. Masquelier, and M. Hervieu, Electronic Crystallization in a Lithium Battery Material: Columnar Ordering of Electrons and Holes in the Spinel LiMn_2O_4 , *Phys. Rev. Lett.* **81**, 4660 (1998).
 - [11] R. Huang, Y. Ikuhara, T. Mizoguchi, S. Findlay, A. Kuwabara, C. Fisher, H. Moriwake, H. Oki, T. Hirayama, and Y. Ikuhara, *Angew. Chem., Int. Ed.* **50**, 3053 (2011).
 - [12] A. Wills, N. Raju, and J. Greedan, *Chem. Mater.* **11**, 1510 (1999).
 - [13] G. Zhong, Y. Wang, X. Zhao, Q. Wang, Y. Yu, and C. Chen, *J. Power Sources* **215**, 368 (2012).
 - [14] J. Molenda, J. Marzec, K. Swierczek, D. Palubiak, W. Ojczyk, and M. Ziernicki, *Solid State Ionics* **175**, 297 (2004).
 - [15] Z. Moorhead-Rosenberg, K. Chemelewski, J. Goodenough, and A. Manthiram, *J. Mater. Chem. A* **1**, 10745 (2013).
 - [16] T. Muraliganth and A. Manthiram, Understanding the Shifts in the Redox Potentials of Olivines $\text{LiM}_{1-y}\text{M}_y\text{PO}_4$ ($\text{M} = \text{Fe}, \text{Mn}, \text{Co}$, and Mg) Solid Solution Cathodes, *J. Phys. Chem. C* **114**, 15530 (2010).
 - [17] A. Manthiram, K. Chemelewski, and L. Eun-Sung, *Energy Environ. Sci.* **7**, 1339 (2014).
 - [18] R. Amin, N. Muralidharan, R. Petla, H. Yahia, S. Al-Hail, R. Essehli, C. Daniel, M. Khaleel, and I. Belharouak, *J. Power Sources* **467**, 228318 (2020).
 - [19] P. Stübke, V. Mereacre, H. Geßwein, and J. Binder, On the Composition of $\text{LiNi}_{0.5}\text{Mn}_{1.5}\text{O}_4$ Cathode Active Materials, *Adv. Energy Mater.* **13**, 2203778 (2023).
 - [20] N. Amdouni, K. Zaghib, F. Gendron, A. Mauger, and C. Julien, *J. Magn. Magn. Mater.* **309**, 100 (2007).
 - [21] Z. Moorhead-Rosenberg, D. Shin, K. Chemelewski, J. Goodenough, and A. Manthiram, *Appl. Phys. Lett.* **100**, 213909 (2012).
 - [22] K. Momma and F. Izumi, VESTA: a three-dimensional visualization system for electronic and structural analysis, *J. Appl. Crystallogr.* **41**, 653 (2008).
 - [23] P. Hohenberg and W. Kohn, Inhomogeneous electron gas, *Phys. Rev.* **136**, B864 (1964).

- [24] W. Kohn and L. Sham, Self-consistent equations including exchange and correlation effects, *Phys. Rev.* **140**, A1133 (1965).
- [25] V. Anisimov, J. Zaanen, and O. Andersen, Band theory and Mott insulators: Hubbard U instead of Stoner I , *Phys. Rev. B* **44**, 943 (1991).
- [26] A. Liechtenstein, V. Anisimov, and J. Zaanen, Density-functional theory and strong interactions: Orbital ordering in Mott-Hubbard insulators, *Phys. Rev. B* **52**, R5467 (1995).
- [27] S. Dudarev, G. Botton, S. Savrasov, C. Humphreys, and A. Sutton, Electron-energy-loss spectra and the structural stability of nickel oxide: An LSDA+ U study, *Physical Review B* **57**, 1505 (1998).
- [28] C. Ouyang, S. Shi, and M. Lei, *J. Alloys Compd.* **474**, 370 (2009).
- [29] B. Xu and S. Meng, *J. Power Sources* **195**, 4971 (2010).
- [30] A. Karim, S. Fosse, and K. Persson, *Phys. Rev. B* **87**, 075322 (2013).
- [31] K. Hoang, *J. Mater. Chem. A* **2**, 18271 (2014).
- [32] W.-W. Liu, D. Wang, Z. Wang, J. Deng, W.-M. Lau, and Y. Zhang, *Phys. Chem. Chem. Phys.* **19**, 6481 (2017).
- [33] E. Isaacs, S. Patel, and C. Wolverton, Prediction of Li intercalation voltages in rechargeable battery cathode materials: Effects of exchange-correlation functional, van der Waals interactions, and Hubbard U , *Phys. Rev. Materials* **4**, 065405 (2020).
- [34] M. Eckhoff, P. Blöchl, and J. Behler, Hybrid density functional theory benchmark study on lithium manganese oxides, *Phys. Rev. B* **101**, 205113 (2020).
- [35] K. Miwa, *Phys. Rev. B* **97**, 075143 (2018).
- [36] V. L. Campo Jr and M. Cococcioni, Extended DFT+ U + V method with on-site and inter-site electronic interactions, *J. Phys.: Condens. Matter* **22**, 055602 (2010).
- [37] N. Tancogne-Dejean and A. Rubio, Parameter-free hybridlike functional based on an extended Hubbard model: DFT+ U + V , *Phys. Rev. B* **102**, 155117 (2020).
- [38] S.-H. Lee and Y.-W. Son, First-principles approach with a pseudohybrid density functional for extended Hubbard interactions, *Phys. Rev. Research* **2**, 043410 (2020).
- [39] H. Kulik and N. Marzari, Transition-metal dioxides: A case for the intersite term in Hubbard-model functionals, *J. Chem. Phys.* **134**, 094103 (2011).
- [40] M. Cococcioni and N. Marzari, Energetics and cathode voltages of LiMPO_4 olivines ($M=\text{Fe, Mn}$) from extended Hubbard functionals, *Phys. Rev. Materials* **3**, 033801 (2019).
- [41] C. Ricca, I. Timrov, M. Cococcioni, N. Marzari, and U. Aschauer, Self-consistent DFT+ U + V study of oxygen vacancies in SrTiO_3 , *Phys. Rev. Research* **2**, 023313 (2020).
- [42] I. Timrov, P. Agrawal, X. Zhang, S. Erat, R. Liu, A. Braun, M. Cococcioni, M. Calandra, N. Marzari, and D. Passerone, Electronic structure of Ni-substituted LaFeO_3 from near edge x-ray absorption fine structure experiments and first-principles simulations, *Phys. Rev. Research* **2**, 033265 (2020).
- [43] R. Mahajan, I. Timrov, N. Marzari, and A. Kashyap, Importance of intersite Hubbard interactions in $\beta\text{-MnO}_2$: A first-principles DFT+ U + V study, *Phys. Rev. Materials* **5**, 104402 (2021).
- [44] R. Mahajan, A. Kashyap, and I. Timrov, Pivotal Role of Intersite Hubbard Interactions in Fe-Doped $\alpha\text{-MnO}_2$, *J. Phys. Chem. C* **126**, 14353 (2022).
- [45] I. Timrov, F. Aquilante, M. Cococcioni, and N. Marzari, *PRX Energy* **1**, 033003 (2022).
- [46] L. Binci, M. Kotiuga, I. Timrov, and N. Marzari, arXiv:2212.12529 (2022).
- [47] W. Yang, S.-H. Jhi, S.-H. Lee, and Y.-W. Son, *Ab initio* Study of Lattice Dynamics of Group IV Semiconductors using Pseudohybrid Functionals for Extended Hubbard Interactions, *Phys. Rev. B* **104**, 104313 (2021).
- [48] B. Jang, M. Kim, S.-H. Lee, W. Yang, S.-H. Jhi, and Y.-W. Son, arXiv:2205.02470.
- [49] W. Yang, B. Jang, Y.-W. Son, and S.-H. Jhi, Lattice Dynamical Properties of Antiferromagnetic Oxides Calculated using Self-consistent Extended Hubbard Functional Method, *J. Phys.: Condens. Matter* **34**, 295601 (2022).
- [50] I. Timrov, N. Marzari, and M. Cococcioni, Hubbard parameters from density-functional perturbation theory, *Phys. Rev. B* **98**, 085127 (2018).
- [51] I. Timrov, N. Marzari, and M. Cococcioni, Self-consistent Hubbard parameters from density-functional perturbation theory in the ultrasoft and projector-augmented wave formulations, *Phys. Rev. B* **103**, 045141 (2021).
- [52] H. Hsu, K. Umemoto, M. Cococcioni, and R. Wentzcovitch, First-Principles Study for Low-Spin LaCoO_3 with a Structurally Consistent Hubbard U , *Phys. Rev. B* **79**, 125124 (2009).
- [53] M. Cococcioni and S. de Gironcoli, Linear response approach to the calculation of the effective interaction parameters in the LDA+ U method, *Phys. Rev. B* **71**, 035105 (2005).
- [54] M. Cococcioni and S. de Gironcoli, Linear response approach to the calculation of the effective interaction parameters in the lda+ u method, *Physical Review B* **71**, 035105 (2005).
- [55] C. Tablero, Representations of the occupation number matrix on the LDA/GGA+ U method, *J. Phys.: Condens. Matter* **20**, 325205 (2008).
- [56] I. Timrov, F. Aquilante, L. Binci, M. Cococcioni, and N. Marzari, Pulay forces in density-functional theory with extended Hubbard functionals: from nonorthogonalized to orthogonalized manifolds, *Phys. Rev. B* **102**, 235159 (2020).
- [57] P.-O. Löwdin, On the Non-Orthogonality Problem Connected with the Use of Atomic Wave Functions in the Theory of Molecules and Crystals, *J. Chem. Phys.* **18**, 365 (1950).
- [58] I. Mayer, On Löwdin's method of symmetric orthogonalization, *Int. J. Quant. Chem.* **90**, 63 (2002).
- [59] B. Amadon, F. Jollet, and M. Torrent, γ and β cerium: LDA+ U calculations of ground-state parameters, *Phys. Rev. B* **77**, 155104 (2008).
- [60] K. Nawa, T. Akiyama, T. Ito, K. Nakamura, T. Oguchi, and M. Weinert, *Phys. Rev. B* **97**, 035117 (2018).
- [61] Y.-C. Wang, Z.-H. Chen, and H. Jiang, The local projection in the density functional theory plus U approach: A critical assessment, *J. Chem. Phys.* **144**, 144106 (2016).
- [62] P. Giannozzi, S. Baroni, N. Bonini, M. Calandra, R. Car, C. Cavazzoni, D. Ceresoli, G. Chiarotti, M. Cococcioni, I. Dabo, A. Dal Corso, S. De Gironcoli, S. Fabris, G. Fratesi, R. Gebauer, U. Gerstmann, C. Gougous-

- sis, A. Kokalj, M. Lazzeri, L. Martin-Samos, N. Marzari, F. Mauri, R. Mazzarello, S. Paolini, A. Pasquarello, L. Paulatto, C. Sbraccia, S. Scandolo, G. Sclauzero, A. Seitsonen, A. Smogunov, P. Umari, and R. Wentzcovitch, Quantum ESPRESSO: A modular and open-source software project for quantum simulations of materials, *J. Phys.: Condens. Matter* **21**, 395502 (2009).
- [63] P. Giannozzi, O. Andreussi, T. Brumme, O. Bunau, M. Buongiorno Nardelli, M. Calandra, R. Car, C. Cavazzoni, D. Ceresoli, M. Cococcioni, N. Colonna, I. Carnimeo, A. Dal Corso, S. de Gironcoli, P. Delugas, R. A. DiStasio Jr., A. Ferretti, A. Floris, G. Fratesi, G. Fugallo, R. Gebauer, U. Gerstmann, F. Giustino, T. Gorni, J. Jia, M. Kawamura, H.-Y. Ko, A. Kokalj, E. Küçükbenli, M. Lazzeri, M. Marsili, N. Marzari, F. Mauri, N. L. Nguyen, H.-V. Nguyen, A. Otero-de-la Rosa, L. Paulatto, S. Poncé, D. Rocca, R. Sabatini, B. Santra, M. Schlipf, A. Seitsonen, A. Smogunov, I. Timrov, T. Thonhauser, P. Umari, N. Vast, and S. Baroni, Advanced capabilities for materials modelling with Quantum ESPRESSO, *J. Phys.: Condens. Matter* **29**, 465901 (2017).
- [64] P. Giannozzi, O. Baseggio, P. Bonfà, D. Brunato, R. Car, I. Carnimeo, C. Cavazzoni, S. de Gironcoli, P. Delugas, F. Ferrari Ruffino, A. Ferretti, N. Marzari, I. Timrov, A. Urru, and S. Baroni, Quantum ESPRESSO toward the exascale, *J. Chem. Phys.* **152**, 154105 (2020).
- [65] A. Kuwabara, C. Fisher, Y. Ikuhara, H. Moriwake, H. Oki, and Y. Ikuhara, *RSC Advances* **2**, 12940 (2012).
- [66] D. A. Kitchaev, H. Peng, Y. Liu, J. Sun, J. P. Perdew, and G. Ceder, Energetics of MnO_2 polymorphs in density functional theory, *Physical Review B* **93**, 045132 (2016).
- [67] J. Perdew, A. Ruzsinszky, G. Csonka, O. Vydrov, G. Scuseria, L. Constantin, X. Zhou, and K. Burke, Restoring the Density-Gradient Expansion for Exchange in Solids and Surfaces, *Phys. Rev. Lett.* **100**, 136406 (2008).
- [68] To be more specific, in the following we use the acronym PBEsol+ U in place of DFT+ U , and PBEsol+ U + V in place of DFT+ U + V .
- [69] G. Prandini, A. Marrazzo, I. E. Castelli, N. Mounet, and N. Marzari, Precision and efficiency in solid-state pseudopotential calculations, *npj Computational Materials* **4**, 1 (2018).
- [70] The SSSP library of the Materials Cloud: <https://www.materialscloud.org/discover/sssp/table/precision>.
- [71] K. Garrity, J. Bennett, K. Rabe, and D. Vanderbilt, Pseudopotentials for high-throughput DFT calculations, *Comput. Mater. Sci.* **81**, 446 (2014).
- [72] E. Küçükbenli, M. Monni, B. Adetunji, X. Ge, G. Adedbayo, N. Marzari, S. de Gironcoli, and A. Dal Corso, Projector augmented-wave and all-electron calculations across the periodic table: a comparison of structural and energetic properties, arXiv:1404.3015 (2014).
- [73] N. Marzari, D. Vanderbilt, A. De Vita, and M. Payne, Thermal Contraction and Disordering of the Al(110) Surface, *Phys. Rev. Lett.* **82**, 3296 (1999).
- [74] R. Fletcher, *Practical Methods of Optimization*, 2nd ed. (Wiley, Chichester, 1987).
- [75] I. Timrov, N. Marzari, and M. Cococcioni, HP – A code for the calculation of Hubbard parameters using density-functional perturbation theory, *Comput. Phys. Commun.* **279**, 108455 (2022).
- [76] S. Baroni, S. de Gironcoli, A. Dal Corso, and P. Giannozzi, *Rev. Mod. Phys.* **73**, 515 (2001).
- [77] T. Gorni, I. Timrov, and S. Baroni, *Eur. Phys. J. B* **91**, 249 (2018).
- [78] C. Ricca, I. Timrov, M. Cococcioni, N. Marzari, and U. Aschauer, Self-consistent site-dependent DFT+ U study of stoichiometric and defective SrMnO_3 , *Phys. Rev. B* **99**, 094102 (2019).
- [79] A. Floris, I. Timrov, B. Himmetoglu, N. Marzari, S. de Gironcoli, and M. Cococcioni, *Phys. Rev. B* **101**, 064305 (2020).
- [80] Y. Sun, M. Cococcioni, and R. Wentzcovitch, *Phys. Rev. Materials* **4**, 063605 (2020).
- [81] J.-J. Zhou, J. Park, I. Timrov, A. Floris, M. Cococcioni, N. Marzari, and M. Bernardi, *Phys. Rev. Lett.* **127**, 126404 (2021).
- [82] N. Kirchner-Hall, W. Zhao, Y. Xiong, I. Timrov, and I. Dabo, Extensive Benchmarking of DFT+ U Calculations for Predicting Band Gaps, *Appl. Sci.* **11**, 2395 (2021).
- [83] Y. Xiong, Q. Campbell, J. Fanghanel, C. Badding, H. Wang, N. Kirchner-Hall, M. Theibault, I. Timrov, J. Mondschein, K. Seth, R. Katz, A. Molina Villarino, B. Pamuk, M. Penrod, M. Khan, T. Rivera, N. Smith, X. Quintana, P. Orbe, C. Fennie, S. Asem-Hiablie, J. Young, T. Deutsch, M. Cococcioni, V. Gopalan, H. Abruña, R. Schaak, and I. Dabo, Optimizing accuracy and efficacy in data-driven materials discovery for the solar production of hydrogen, *Energy Environ. Sci.* **14**, 2335 (2021).
- [84] I. Timrov, M. Kotiuga, and N. Marzari, [Unraveling the effects of inter-site Hubbard interactions in spinel Li-ion cathode materials](#), *Materials Cloud Archive* **2023.25** (2023), doi: 10.24435/materialscloud:ry-v5.
- [85] Y. Jang, B. Huang, F. Chou, D. Sadoway, and Y. Chiang, *J. Appl. Phys.* **87**, 7382 (2000).
- [86] W. Kan, S. Kuppan, L. Cheng, M. Doeff, J. Nanda, A. Huq, and G. Chen, *Chem. Mater.* **29**, 6818 (2017).
- [87] P. H.-L. Sit, R. Car, M. H. Cohen, and A. Selloni, Simple, Unambiguous Theoretical Approach to Oxidation State Determination via First-Principles Calculations, *Inorg. Chem.* **50**, 10259 (2011).
- [88] H. Raebiger, S. Lany, and A. Zunger, Charge self-regulation upon changing the oxidation state of transition metals in insulators, *Nature* **453**, 763 (2008).
- [89] R. Resta, Charge states in transition, *Nature* **453**, 735 (2008).
- [90] J. Reed and G. Ceder, Charge, Potential, and Phase Stability of Layered $\text{Li}(\text{Ni}_{0.5}\text{Mn}_{0.5})\text{O}_2$, *Electrochem. Solid-State Lett.* **5**, A145 (2002).
- [91] J. Perdew and A. Zunger, Self-interaction correction to density-functional approximations for many-electron systems, *Phys. Rev. B* **23**, 5048 (1981).
- [92] P. Mori-Sánchez, A. Cohen, and W. Yang, Many-electron self-interaction error in approximate density functionals, *J. Chem. Phys.* **125**, 201102 (2006).
- [93] H. Kulik, M. Cococcioni, D. Scherlis, and N. Marzari, Density Functional Theory in Transition-Metal Chemistry: A Self-Consistent Hubbard U Approach, *Phys. Rev. Lett.* **97**, 103001 (2006).
- [94] H. Kulik and N. Marzari, A self-consistent Hubbard U density-functional theory approach to the addition-

- elimination reactions of hydrocarbons on bare FeO^+ , J. Chem. Phys. **129**, 134314 (2008).
- [95] C. Ouyang, H. Deng, Z. Ye, M. Lei, and L. Chen, This Solid Films **503**, 268 (2006).
 - [96] B. Singh, S. Kumar, and P. Kumar, Broken translational and rotational symmetries in $\text{LiMn}_{1.5}\text{Ni}_{0.5}\text{O}_4$ spinel, J. Phys.: Condens. Matter **31**, 395701 (2019).
 - [97] M. Aydinol, A. Kohan, G. Ceder, K. Cho, and J. Joannopoulos, *Ab initio* study of lithium intercalation in metal oxides and metal dichalcogenides, Phys. Rev. B **56**, 1354 (1997).
 - [98] T. B lle, N. Mathiesen, A. Nielsen, T. Vegge, J. Garcia-Lastra, and I. Castelli, Batteries & Supercaps **3**, 488 (2020).
 - [99] M. Aydinol, A. Kohan, and G. Ceder, *Ab initio* calculation of the intercalation voltage of lithium-transition-metal oxide electrodes for rechargeable batteries, J. Power Sources **68**, 664 (1997).
 - [100] Q. Zhong, A. Bonakdarpour, M. Zhang, Y. Gao, and J. Dahn, J. Electrochem. Soc. **144**, 205 (1997).